H$_2$ and CO heterogeneous kinetic coupling during combustion of H$_2$/CO/O$_2$/N$_2$ mixtures over rhodium

Ran Sui [a,1], John Mantzaras [a,*], Rolf Bombach [b]

[a] *Laboratory for Scientific Computing and Modeling, Paul Scherrer Institute, CH-5232 Villigen PSI, Switzerland*
[b] *Energy System Integration Platform, Paul Scherrer Institute, CH-5232 Villigen PSI, Switzerland*

A B S T R A C T

The chemical interactions between CO and H$_2$ over rhodium were investigated for H$_2$/CO/O$_2$/N$_2$ mixtures with H$_2$:CO volumetric ratios 1:5–3:1, overall fuel-lean equivalence ratios $\varphi = 0.13$ and 0.23, a pressure of 5 bar, and surface temperatures 510-610 K. This temperature range was particularly important for catalytic ignition in hybrid hetero-/homogeneous combustion concepts of large gas-turbines operating at part-load or idling conditions and in recuperative micro-turbine-based microreactors at normal operation. In situ Raman measurements of major gas-phase species concentrations were carried out over the catalyst boundary layer, while 2-D simulations were performed with a detailed catalytic reaction scheme. Comparisons of simulations and measurements assessed the performance of the catalytic reaction mechanism for the oxidation of pure CO, pure H$_2$ and H$_2$/CO fuel blends. Transition temperatures were identified below (above) which H$_2$ inhibited (promoted) the oxidation of CO. For a given equivalence ratio, the transition temperatures decreased significantly with increasing H$_2$:CO volumetric ratio (595 K for H$_2$:CO $= 1$:5 and less than 535 K for H$_2$:CO $= 3$:1, at $\varphi = 0.13$) while for a given H$_2$:CO volumetric ratio they dropped moderately with decreasing φ. This behavior was fundamentally different to that of platinum catalysts, whereby transition temperatures depended weakly on H$_2$:CO volumetric ratio and stronger on equivalence ratio. The strong dependence of the transition temperatures on H$_2$:CO volumetric ratio over rhodium pointed to the advantage of this catalyst when used for high-hydrogen-content ($> 80\%$ volume) fuels in power generation applications. The promotion effect of H$_2$ on CO oxidation above the transition temperatures was a result of the increased importance of the indirect CO oxidation route via surface COOH.

1. Introduction

Combustion technologies with reduced greenhouse gas emissions are currently under intense investigation for large-scale power generation systems. In integrated gasification combined cycle (IGCC) approaches [1], pre-combustion CO$_2$ capture is achieved by gasifying solid and liquid fossil fuels and converting them to syngas, a gas comprising mainly H$_2$ and CO. A water gas shift (WGS) reactor can further increase the hydrogen content in the produced syngas. Apart from liquid and solid fuels, pre-combustion CO$_2$ capture can be applied to natural-gas-fueled turbines by reforming the natural gas to syngas [2,3]. In addition to large power plants, low CO$_2$ footprint syngas and biogas fuels are also attractive for microreactors used for portable power generation [4,5].

Catalytically stabilized thermal combustion (CST) is a hybrid approach whereby part of the fuel is combusted heterogeneously in an upstream catalytic reactor (typically coated with a noble metal) and the remaining fuel is converted homogeneously in a follow-up flame zone [6–8]. Hybrid combustion methodologies are well suited for large-scale power generation when using syngas or pure hydrogen fuels [9–11]. This is because conventional lean-premixed gaseous combustion of high-hydrogen-content fuels is prone to flashback, whereas in CST the upstream catalytic reactor mitigates this risk due to the inhibiting effect of heterogeneous reactions on gaseous combustion and flame propagation [12]. Furthermore, hetero-/homogeneous combustion allows for ultra-low NOx emissions as the catalytic reaction pathway does not produce the radicals driving the NOx formation mechanism [13,14]. Pure catalytic combustion and hybrid hetero-/homogeneous combustion methodologies are also of interest for microreactors due to their large surface-to-volume ratios that favor heterogeneous surface reactions

Nomenclature

b	channel half-height, Figs. 1 and 2
$D_{k,m}$	mixture-average diffusion coefficient of kth gaseous species, Eq. (3)
D_k^T	thermal diffusion coefficient of kth gaseous species, Eq. (3)
K_g	total number of gaseous species, Eqs. (1) and ((3))
L	catalytic channel length, Figs. 1 and 2
Le	Lewis number (thermal over mass diffusivity)
p	pressure
Re_{IN}	inlet Reynolds number
$\dot{s}_k$	catalytic molar production rate of kth species, Eq. (1)
T	temperature
U_{IN}	inlet streamwise velocity
$\vec{V}_k$	diffusion velocity vector of kth gaseous species, Eq. (3)
W	catalytic channel width, Figs. 1 and 2
W_k	molecular weight of kth gaseous species, Eq. (1)
X_k, Y_k	mole fraction and mass fraction of kth gaseous species
x, y, z	streamwise, transverse and lateral coordinates, Fig. 1

Greek Symbols

α_{H2}, α_{CO}	ratio of fuel volume to fuel and oxygen volume, Fig. 12
ρ	gas density, Eqs. (1) and (3)
φ	fuel-to-oxygen equivalence ratio

Subscripts

IN	inlet
ig	catalytic ignition
TRAN	transition
W	wall
U, L	upper and lower walls

and the effective suppression of undesirable flame instabilities due to the presence of a catalyst [15,16]. Therefore, understanding the kinetic interactions of H_2 and CO over noble metal catalysts is cardinal for the development of catalytic syngas combustors for either large-scale or small-scale power systems.

The catalytic kinetic interactions between CO and H_2 in the temperature range ~500–650 K are of main interest for part-load and idling operation in large gas turbines and also for normal operation in microreactors employing recuperative micro-turbines [17]. For platinum catalysts, intricate kinetic interactions have been observed at fuel-lean H_2/CO/air overall stoichiometries (i.e. based on both fuel components). Salomons et al. [18] reported that addition of H_2 promoted the CO oxidation on Pt in a nonlinear fashion, whereas Federici and Vlachos [19] observed neutral H_2 effects for H_2:CO volumetric ratios larger than unity and promoting H_2 effects at lower H_2:CO ratios. Simulations in Mantzaras [9] have shown an inhibiting effect of H_2 on CO oxidation over Pt below a critical temperature ~580 K which, however, strongly depended on the particular surface reaction mechanism. Recent advances in laser-based in situ measurements of gas-phase thermoscalars above catalytic surfaces have allowed for assessing the underlying catalytic and gas-phase chemical processes [20]. To this direction, Raman measurements of major gaseous species concentrations above Pt-coated surfaces were performed in [21,22] for H_2/CO/O_2/N_2 mixtures with overall equivalence ratios 0.13 and 0.26, H_2:CO molar ratios 1:5–3:1 and a constant pressure of 5 bar. Transition temperatures in the range 550–600 K were established [22] below which

the addition of H_2 chemically inhibited the oxidation of CO. This inhibition was due to the competition between H_2, CO and O_2 for adsorption on Pt free sites and, more importantly, due to the competition between the adsorbed H(s) and CO(s) surface species for surface-deficient O(s).

In power generation, Pd and bimetallic Pd/Pt are the preferred noble metal catalysts [7,23] since natural gas is the main fuel of interest and Pd has the highest activity towards methane total oxidation. However, Rh catalysts can be used as additives or promoters in other noble metals. For example, addition of Rh into Pt enhances the activity of Pt in the total oxidation of methane [24] whereas the addition of Rh on Pd increases the stability of Pd without appreciably changing its activity [25]. For the surface oxidation of H_2/CO fuel blends, the benefits of Rh catalysts have not been fully explored. The kinetics of the individual H_2 and CO fuel components on Rh has been studied in [26–29]. The oxidation of H_2/CO mixtures was also investigated in [26], focusing on the CO preferential oxidation (PROX) whereby only small amounts of CO ($\leq$ 1% volume) were present in the syngas. However, in power generation systems and depending on the syngas provenance, CO contents could be much higher (e.g. 30–60% per volume in coal gasification). It is hence of main interest to study the H_2/CO kinetic interactions under diverse H_2/CO compositions.

The present study undertakes an investigation of the H_2/CO oxidation over Rh at temperatures 510-610 K, which are relevant for catalytic ignition in power generation systems. Experiments were carried out in an optically accessible Rh-coated channel-flow reactor, equipped with a dedicated cooling system in order to attain the desired modest operating temperatures. In situ Raman measurements of major gas-phase species concentrations over the channel catalytic surfaces were performed at a pressure of 5 bar, two overall fuel-to-oxygen equivalence ratios (0.13 and 0.23), and H_2:CO volumetric ratios in the range 1:5-3:1. Surface science analysis by means of X-ray photoelectron spectroscopy (XPS) and scanning electron microscopy (SEM) determined the oxidation state and surface morphology of the catalyst, respectively. A 2-D code with a detailed catalytic chemical reaction scheme and realistic transport simulated the experiments. Main objectives were to study the catalytic chemical interactions between the H_2 and CO fuel components and to identify the minimum temperatures required to avoid H_2 inhibition on CO oxidation. Specific objective was to compare performances with other noble metal catalysts and to propose catalyst selection strategies for the start-up of relevant power generation systems.

This article is organized as follows. The experimental setup and measuring techniques are introduced in Section 2 while the numerical methodology is presented in Section 3. Comparisons between measurements and simulations for pure H_2 and CO follow in Section 4.1, H_2/CO blends and the kinetic coupling between H_2 and CO is elaborated in Section 4.2, surface science results are discussed in Section 4.3 and the impact of the kinetic coupling on the ignition characteristics of practical catalytic reactors is addressed in Section 4.4. Main results are summarized in Section 5.

2. Experimental

2.1. Test rig and catalytic reactor

The reactor and high pressure test-rig have been detailed in [22,30], however, essential changes were necessary to accommodate the present moderate-temperature experiments. The catalytic reactor (see Fig. 1) comprised two horizontal Si[SiC] ceramic plates and two vertical quartz windows (each 300 mm long, 3 mm thick, and 12 mm high). Each Si[SiC] plate had a length $L = 300$ mm ($-x$), a full width 110 mm and an inner width $W = 104$ mm ($-z$)

Fig. 1. High pressure test rig with catalytic reactor: (a) side view, (b) cross-flow view. All dimensions are in mm.

Fig. 2. Optical setup of the Raman system. All dimensions and focal lengths are in mm.

(Fig. 1(b)), and a thickness of 9-mm; the two plates were placed at a distance $2b = 7$ mm apart $(-y)$.

Using plasma vapor deposition (PVD), the inner Si[SiC] surfaces were coated first with a 1.5 μm thick nonporous Al_2O_3 layer and then with a 2.2 μm thick rhodium layer. Such thick noble metal layers resembled polycrystalline surfaces, as confirmed earlier [31] and as attested with the present XPS and SEM measurements. In particular, XPS revealed that no Al diffused to the catalyst surface even after extended operation at the investigated temperatures.

The catalytically-coated Si[SiC] plates were supported on an Inconel frame that was in turn mounted inside a high-pressure cylindrical steel tank equipped with two $350 \times 50 \times 35$ mm^3 quartz glass side windows (Fig. 1(b)). For each plate, 12 S-type thermocouples positioned along the x-y symmetry plane of the reactor ($z = 0$, see Fig. 1) monitored the surface temperatures. The thermocouples were embedded 0.9 mm beneath the catalyst surface by means of 1.2 mm diameter and 8.1 mm deep holes eroded from the outer (uncoated) Si[SiC] surfaces. In addition to the central thermocouples, 6 side S-type thermocouples on each plate (Fig. 1(b)) monitored the catalyst surface temperatures at $z = \pm 45$ mm and $x = 12, 80, 142$ mm ($x = 0$ denotes the start of the catalytic plates).

Achieving the desirable modest surface temperatures (< 650 K) at the appreciably-high equivalence ratios $\varphi = 0.13$ and 0.23 was a challenging task, which was further compounded by the low Lewis number of the hydrogen component ($Le_{H2} \sim 0.3$ in air at fuel-lean stoichiometries) that created superadiabatic surface temperatures at the channel entry [32–34]. Hence, a special arrangement with adjustable cooling power was necessary to control the surface temperatures. The front faces of the Si[SiC] plates (110×9 mm^2) were contacted to a water-cooled section of the Inconel support frame (Fig. 1(a)), providing a base cooling power for all experiments. In addition to the base cooling, fine control of the total cooling power was achieved by two room-temperature adjustable jet air flows at $x = 30$ mm (see Fig. 1(a)). The air flows were distributed laterally (z-direction) by means of two 10 mm in diameter by 100 mm long cylindrical tubes, each having 16 holes with progressively

increasing diameters from $d = 1.0$ mm at $z \sim 0$ mm to $d = 2.5$ mm at $z = \pm 50$ mm so as to create uniform vertical velocity flows impinging on the outer Si[SiC] surfaces (see Fig. 1(b)). Despite the water and jet-air impingement cooling at the reactor front, it was still necessary to heat the rear Si[SiC] parts ($100 < x < 300$ mm) with two resistive coils (Fig. 1(a)), otherwise the heat losses to the Inconel support frame would eventually extinguish the catalytic reactions along the entire catalyst length.

High-purity H_2 (99.99%), CO (99.5%), N_2 (99.99%) and O_2 (99.5%) gases were supplied by batteries and their flows were regulated by four Brooks mass flow controllers. Two premixed streams of O_2/N_2 and H_2/CO were formed, and subsequently H_2/CO was injected counterflow to O_2/N_2 by means of eight 0.5 mm diameter nozzles arranged laterally. Further mixing of the two steams of gases occurred in a subsequent 200-mm-long steel conical unit (Fig. 1(a)) that had an ending cross-flow area equal to that of the channel-reactor (104×7 mm^2). A wire mesh and two fine grids (0.5 mm^2) in the conical section ensured good mixing of the H_2/CO and O_2/N_2 flows and a uniform exit velocity. Hot wire velocimetry assessed the flow uniformity at the exit of the stand-alone conical unit, while planar laser induced fluorescence of NO (added into the H_2/CO stream, excitation at 226.25 nm, detection at 240–265 nm) confirmed the good mixing quality. The inlet gas temperature ($x = 0$) was monitored by a K-type sheathed thermocouple, marked TC_D in Fig. 1(a). Three additional sheathed K-type thermocouples (TC_A, TC_B and TC_C in Fig. 1(a)) positioned upstream of the reactor monitored the gas temperature, thus ensuring mitigation of autoignition inside the mixing section and serving as safety control.

2.2. Laser diagnostics

A 2 kHz repetition rate, frequency-doubled Nd:YLF laser (Quantronix Darwin-Duo 80, 526.5 nm, 120 ns pulse width, 40 mJ energy/pulse) provided the excitation for the Raman measurements. The laser beam was focused by an $f = 150$ mm cylindrical lens into a vertical line spanning the 7 mm channel height (Fig. 2). The focus was offset 15 mm laterally (-z) to increase the signal collection angle and minimize thermal beam steering, as in [30,31]. Raman-scattered light was focused with two spherical lenses (f/4, $f = 300$ mm) into the entrance slit of a 25 cm spectrograph (Chromex-250i) equipped with an intensified CCD camera (Princeton-Instruments PI-MAX1024GIII, 715×255 pixels referring to spectral shift and transverse distance, respectively). A tilted Kaiser-Optical-Systems holographic notch filter at 532 nm and an

OG550 Schott colored-glass filter suppressed the excitation radiation.

Given the steady and laminar operating conditions, Raman scattered light of 300,000 laser pulses was integrated on the detector chip to increase the signal-to-noise ratio. Data were acquired over the length $8 \leq x \leq 115$ mm by traversing axially an optical table housing the laser and the sending/collecting optics (Fig. 2). The 7 mm channel-height was resolved by 220 pixels, which were subsequently binned to 64 pixels. The effective Raman cross-sections (including transmission efficiencies for windows, lenses, spectrometer, filters and camera), were assessed by recording the signals of several CO, H_2, O_2, and N_2 mixtures, and the actual feed mixtures as in [22,30]. Measurement accuracy was $\pm 3\%$ for species concentration $\geq 3\%$ volume and $\pm 6\%$ for concentration down to 0.5% volume, while lower concentrations entailed larger uncertainties. Raman data within ~ 0.5-0.7 mm from the catalyst surfaces were discarded due to low signal-to-noise ratios.

2.3. Surface science measurements

For the surface science measurements, 5×5 mm^2 samples were coated with 2.2-μm-thick Rh and 1.5-μm-thick Al_2O_3 layers using exactly the same PVD procedure as for the ceramic plates (Section 2.1). XPS analysis was performed ex situ for one as-prepared sample at 293 K and for four samples heated for 2 hr in atmospheric-pressure air at temperatures of 473, 523, 573 and 623 K (corresponding to the range of surface temperatures obtained in the experiments). XPS measurements were accomplished with a VG ESCALAB 220iXL spectrometer (Thermo Fisher Scientific) using focused monochromatized Al Kα radiation (1486.6 eV). The spectrometer was calibrated using the Ag $3d_{5/2}$ peak with a binding energy of 368.3 eV. The spot size at the sample was about 500 μm in diameter and the analysis chamber had a base pressure of approximately 2×10^{-9} mbar. Spectra were recorded in constant analyzer energy mode with pass energy of 30 eV and energy step of 0.05 eV. The acquired data were analyzed by the CasaXPS software using a sum of Gaussian and Lorentzian functions to fit the peaks and a Shirley algorithm for background subtraction.

For scanning electron microscopy, a SEM-Zeiss ULTRA 55 instrument was used with a secondary electrons (SE) detector to obtain high spatial resolution images of sample morphology. SEM was accompanied by energy dispersive X-ray spectroscopy (EDS) that provided the elemental surface composition, using an EDAX APOLLO XV Silicon Drift Detector.

3. Numerical

A 2-D steady Navier–Stokes code was used [22]. The modest surface temperatures (< 650 K) of interest for the present investigation were attained at $x < 120$ mm such that the first 120 mm channel length has been simulated. A staggered mesh with 320×68 grid points (in x and y, respectively) for the 120×7 mm^2 channel domain yielded grid-independent solutions. The very large cross-flow aspect ratio of the channel ($W: 2b \sim 15:1$) warranted adequacy of the 2-D model as discussed in [33]. Furthermore, the two-dimensionality was preserved by the laterally-uniform impinging air flows on both plates. This was also verified by the side thermocouples at $z = \pm 45$ mm, which deviated from the central ($z = 0$) thermocouple at the same axial position by 9–16 K.

From the detailed methane mechanism on Rh by Karakaya et al. [35] the H_2/CO subset was used (9 surface and 6 gaseous species, 30 reactions, surface site density 2.7×10^{-9} mol/cm^2, see Table SM1 in supplemental material). The CO and H_2 reaction parts have been independently tested in [29] and [36], respectively. Surface temperatures were too low (< 650 K) for gaseous chemistry to be significant. This was also verified by including in the simulations the

Table 1
Experimental conditions[a].

Case	φ	U_{IN}	T_{IN}	H_2	CO	O_2	H_2:CO
1	0.13	0.71	311	0	9.2	34.8	0.0
2	0.23	0.63	312	0	14.2	30.9	0.0
3	0.13	1.11	306	5.9	0.0	22.9	∞
4	0.23	1.09	306	5.9	0.0	12.8	∞
5	0.13	0.62	308	6.1	2.0	31.7	3:1
6	0.13	0.52	308	5.4	2.9	31.7	1.9:1
7	0.13	0.77	308	4.3	4.3	32.9	1:1
8	0.13	1.03	306	2.1	6.4	32.8	1:3
9	0.13	0.72	308	1.4	7.1	32.9	1:5
10	0.23	0.52	310	9.2	3.0	26.8	3:1
11	0.23	0.52	309	6.7	6.7	29.1	1:1
12	0.23	0.72	307	3.6	10.7	31.0	1:3

[a] Equivalence ratio, inlet velocity (m/s), inlet temperature (K), H_2, CO and O_2 volumetric content (%, with balance N_2), and H_2:CO ratio.

gaseous syngas mechanism of Li et al. [37], which had been successfully tested against syngas homogeneous ignition experiments over platinum at wall temperatures larger than 1100 K [10]. Simulations with only catalytic and with combined catalytic/gas chemistry indicated that the major species were unaffected by gaseous chemical reactions.

The governing equations have been provided elsewhere [22,34] and are not repeated here. The inlet properties ($x = 0$) were uniform, while zero-Neumann conditions were imposed at the end of the domain. The interfacial gas-solid boundary conditions for the gaseous species and energy are as follows:

$$-\left(\rho Y_k V_{k,y}\right)_{y=0} + (\dot{s}_k)_{y=0} W_k = 0,$$

$$\left(\rho Y_k V_{k,y}\right)_{y=2b} + (\dot{s}_k)_{y=2b} W_k = 0, \ k = 1, ..K_g, \tag{1}$$

$$T(x, y = 0) = T_{w,L}(x), \ T(x, y = 2b) = T_{w,U}(x), \tag{2}$$

with $T_{w,L}(x)$ and $T_{w,U}(x)$ the temperature profiles along the $z = 0$ plane of symmetry at the lower ($y = 0$) and upper ($y = 2b$) catalytic walls, respectively. These profiles were constructed by fitting curves through the individual thermocouple measurements positioned along $z = 0$. In Eq. (1) a mixture-average diffusion model (including thermal diffusion for the light species H_2 and H) was used, along with the Chemkin transport database [38]:

$$\vec{V}_k = -D_{k,m} \frac{\vec{\nabla} X_k}{X_k} - \frac{D_k^T}{\rho Y_k} \frac{\vec{\nabla} T}{T}, \ k = 1, ...K_g. \tag{3}$$

Catalytic reaction rates were evaluated with Surface-Chemkin [39] and gaseous reaction rates (in cases where gaseous chemistry was included to verify its negligible contribution) with Chemkin [40].

4. Results and discussion

Two overall equivalence ratios ($\varphi = 0.13$ and 0.23, based on both CO and H_2 fuel components) were employed, with H_2:CO volumetric ratios 1:5-3:1 (see Table 1) and a pressure of 5 bar. Pure CO and H_2 fuels were also investigated at equivalence ratios $\varphi = 0.13$ and 0.23 (Cases 1–4). The flows were laminar with inlet Reynolds numbers 900-1820 based on the inlet properties and channel height.

4.1. Combustion of individual CO and H_2 fuel components

Before investigating the catalytic combustion of H_2/CO blends over Rh, the combustion of the individual fuel components is first addressed so as to ensure that the adopted reaction mechanism reproduces the oxidation characteristics of H_2 and CO. Measured and predicted traverse profiles of CO mole fractions are shown in
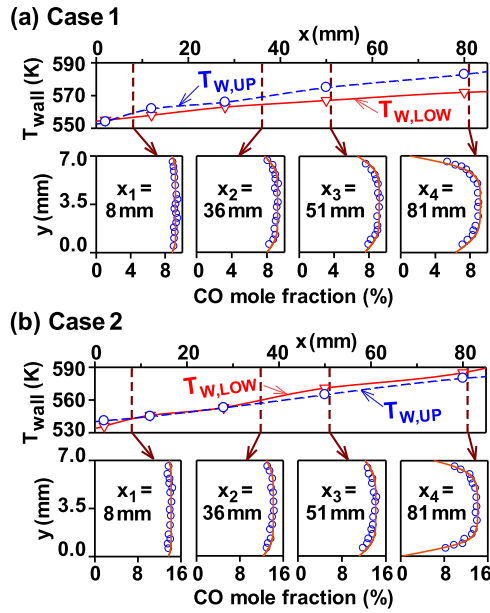
Fig. 3. Measured wall temperatures (circles: upper-wall, triangles: lower-wall) with fitted wall temperature profiles (lines), and comparisons between Raman-measured (symbols) and predicted (lines) transverse profiles of CO mole fractions at four axial positions: (a) Case 1, and (b) Case 2 in Table 1.

Fig. 3 at four selected axial positions x_1-x_4, for Cases 1 and 2 with only CO fuel. For clarity, up to 18 of the total 64 Raman data points are shown over the resolvable transverse extent $0.6 \lesssim y \lesssim 6.4$ mm. The upper-wall and lower-wall temperature profiles are also included in Fig. 3. The predicted CO profiles were in good agreement with the Raman measurements, capturing the near-wall bending and hence the transverse gradient of the deficient CO reactant at the wall, which was a quantity directly linked to the local catalytic reaction rate [20,22]. A kinetically-controlled CO conversion was evident in Fig. 3(a) at all axial positions and in Fig. 3(b) at x_1, x_2 and x_3 (therein, the CO mole fractions were well-above zero at both catalytic walls). The CO catalytic conversion shifted from kinetically-controlled to transport-controlled in Fig. 3(b) at the last axial position $x_4 = 81$ mm and at the lower wall ($y = 0$), as manifested by the computed vanishing CO mole fraction at this position. The measurements corroborated this behavior, despite the lack of Raman data within ∼0.6 mm from both catalytic walls.

A qualitative argument for the dependence of the catalytic reactivity on the CO content could readily be inferred from Fig. 3, by noticing that the transverse wall gradients of the CO mole fractions were similar in magnitude for Cases 1 and 2. The computed magnitudes of these gradients, $|\partial X_{CO}/\partial y|_{y=0,2b}$, were within 14–19% for Cases 1 and 2, when comparing axial positions having wall temperatures differing by less than 4 K. Such comparisons were possible, as the wall temperatures in Cases 1 and 2 were quite similar (see Fig. 3) and deviated by 2–15 K over the extent $x_1 \leq x \leq x_4$. Given the nearly 60% higher CO mole fraction in Case 2 compared to Case 1, a largely neutral dependence of the catalytic reactivity on CO content was obtained. This could be deduced from Eqs. (1) and (3) which, by neglecting the thermal diffusion term for CO, yield $|\partial X_{CO}/\partial y|_{y=0,2b} \sim |\dot{s}_{CO}|_{y=0,2b}$. Assuming an overall reaction rate depending on the CO concentration according to $|\dot{s}_{CO}|_{y=0,2b} \sim [CO]^{\beta}$ it is evident that the near constancy of $|\partial X_{CO}/\partial y|_{y=0,2b}$ and hence of $|\dot{s}_{CO}|_{y=0,2b}$ necessitated an exponent β close to zero. This finding was in agreement with recent literature on CO oxidation over Rh [41]. While it has been established that CO self-inhibits its ignition on Rh [26,41] (i.e. larger ratios $\alpha_{CO} = X_{CO}/(X_{CO}+X_{O2})$ lead to higher ignition tem-
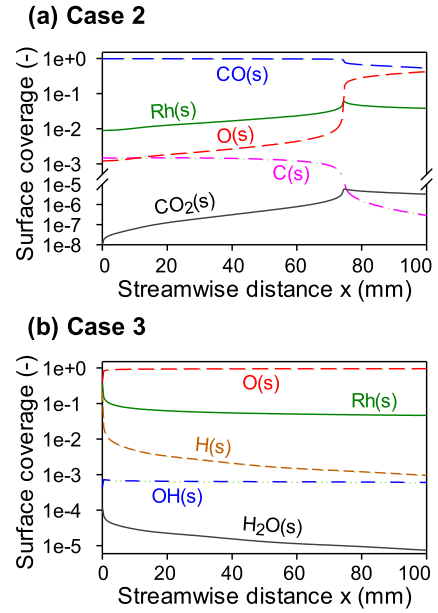
Fig. 4. Surface coverage at the lower wall: (a) Case 2 and (b) Case 3.
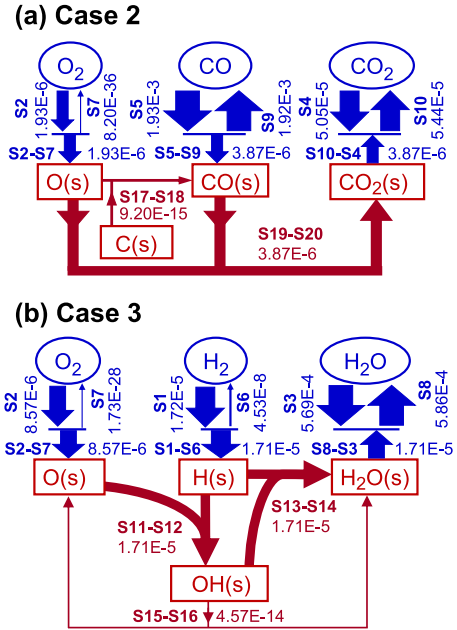
Fig. 5. Reaction flux diagrams at $x = 51$ mm, lower wall: (a) Case 2 and (b) Case 3 (units: mol/cm²s).

peratures and hence to negative exponents β), this inhibition diminishes for $\alpha_{CO} < 0.4$ such that a nearly α_{CO}-independent ignition behavior was reported in [41]. Cases 1 and 2 in Fig. 3 had sufficiently low $\alpha_{CO} = 0.21$ and 0.31, respectively, such that their similar reaction rates were consistent with the findings in [41].

The surface coverage for Case 2 at the lower wall is plotted in Fig. 4(a) and indicates CO(s) as the main surface species, especially over the length $x \lesssim 75$ mm where the CO conversion was kinetically-controlled. However, as the CO reactions became fully ignited (transport limited CO conversion, e.g. the lower wall position $x_4 = 81$ mm in Fig. 3(b)) the O(s) coverage increased at the expense of CO(s). The reaction flux diagram for Case 2 at location $x = 51$ mm of the lower wall is shown in Fig. 5(a). Adsorption of CO and O_2 was favored against desorption of these species; furthermore, at the present modest wall temperatures the dissociative
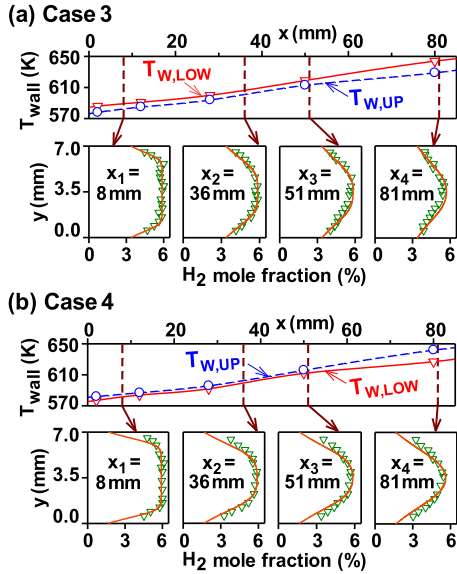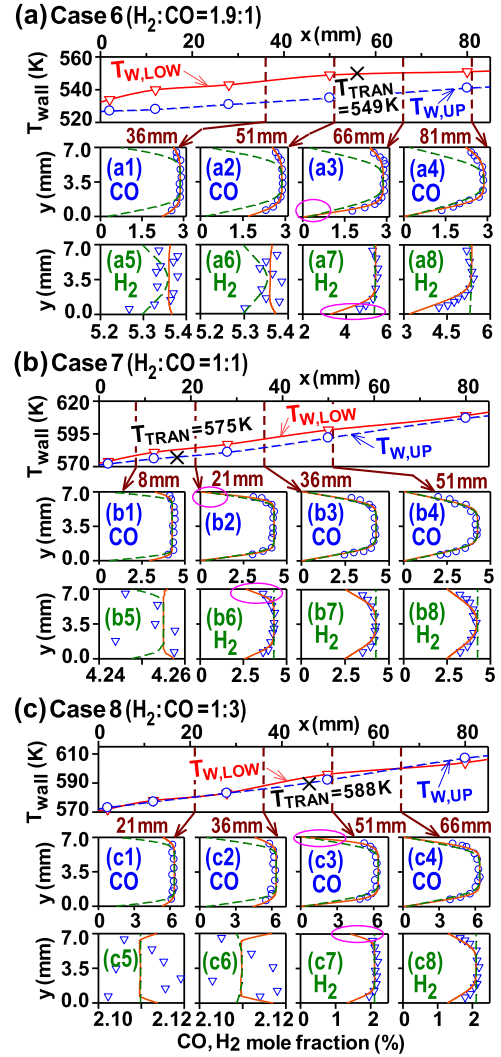
Fig. 6. Measured wall temperatures (circles: upper-wall, triangles: lower-wall) with fitted temperature profiles (lines), and comparisons between Raman-measured (symbols) and predicted (lines) transverse profiles of H_2 mole fractions at four axial positions: (a) Case 3 and (b) Case 4 in Table 1.

adsorption of O_2 was essentially irreversible (see magnitudes of the adsorption and desorption reactions S2 and S7, respectively, in Fig. 5(a)).

Comparisons between measured and predicted transverse profiles of H_2 mole fraction and measured wall temperature profiles for the only-H_2 Cases 3 and 4 are shown in Fig. 6. For each of the two cases, the magnitudes of transverse wall gradients $|\partial X_{H2}/\partial y|_{y=0.2b}$ dropped with increasing x-distance despite the corresponding wall temperature rise (from ~580 K to ~640 K). Furthermore, transport-limited conditions (i.e. fully-ignited states) were never attained. The simulations indicated that this was an outcome of the competition between O_2 and H_2 for adsorption, with the O(s) coverage increasing from 0.83 ($x = 0$) to 0.96 ($x = 81$ mm) in Cases 3 and 4 (see Fig. 4(b)) thus progressively blocking the adsorption of H_2. These results were consistent to literature, since for the low $\alpha_{H2} = X_{H2}/(X_{H2}+X_{O2})$ ratios 0.21 and 0.32 of Cases 3 and 4, respectively, hydrogen ignition temperatures on Rh were reported to be higher than those of CO (when comparing the same α_{CO} and α_{H2} ratios) and could even exceed 650 K [41]. The reaction flux diagram for Case 3 at $x = 51$ mm of the lower wall (Fig. 5(b)) illustrated that the dissociative adsorption reactions of O_2 and H_2 were strongly irreversible at the present temperatures (compare magnitudes of S2 with S7 and of S1 with S6).

The steeper wall gradients $|\partial X_{H2}/\partial y|_{y=0.2b}$ in Case 4 compared to Case 3 (see Fig. 6), in conjunction with the very similar wall temperatures of the two cases (they differed by only 1–5 K), pointed to a higher reactivity for Case 4 with the higher α_{H2}. This was again consistent with the reported self-promotion of hydrogen ignition on Rh (increasing α_{H2} decreased the ignition temperatures), an effect becoming more pronounced at lower α_{H2} [26,41]. The self-promoting ignition of H_2 was in contrast to the aforementioned self-inhibition of CO on rhodium and also to the self-inhibition of H_2 on platinum [42]. The agreement between measurements and simulations in Fig. 6 was good, although in Case 4 the H_2 reactivity was slightly overpredicted.

4.2. Combustion of H_2/CO mixtures

Measured and predicted transverse profiles of CO and H_2 mole fractions and measured wall temperature profiles are provided in

Fig. 7. Measured wall temperatures (circles: upper-wall, triangles: lower-wall) with fitted profiles (lines), and comparisons between Raman-measured (symbols) and predicted (solid lines) transverse profiles of CO and H_2 mole fractions for: (a) Case 6, (b) Case 7 and (c) Case 8. Dashed lines in the CO plots denote predictions by replacing H_2 with an artificial inert H_2^* species, while dashed lines in the H_2 plots denote predictions by replacing CO with an artificial inert CO* species. Symbols (×) mark transition temperatures.

Fig. 7 for Cases 6–8 with equivalence ratio $\varphi = 0.13$. To facilitate the ensuing discussion on H_2/CO chemical interactions, additional simulations for the CO mole fractions (dashed lines in Fig. 7(a1–a4, b1–b4, c1–c4)) are included, which have been carried out by replacing H_2 with an artificial species H_2^* that had the same thermodynamic and transport properties as H_2 but was chemically inert. Alternately, additional simulations for the H_2 mole fractions (dashed lines in Fig. 7(a5–a8, b5–b8, c5–c8)) were obtained by replacing CO with an artificial species CO* that had the same thermodynamic and transport properties as CO but was chemically inert. The CO measurements and normal predictions (solid lines) were in good agreement with each other. Furthermore, for H_2 and at all axial positions that exhibited a kinetically-controlled hydrogen conversion (e.g. Fig. 7(a7–a8, b6–b8, c7–c8)) the agreement with measurements was also good, although the H_2 catalytic reactivity was somewhat overpredicted (steeper predicted near-wall gradients $|\partial X_{H2}/\partial y|$).

At the upstream axial positions in Fig. 7(a5–a6, b5, c5–c6) the H_2 catalytic reactivity was practically zero, such that the horizontal axes have been greatly stretched to exemplify the near-wall
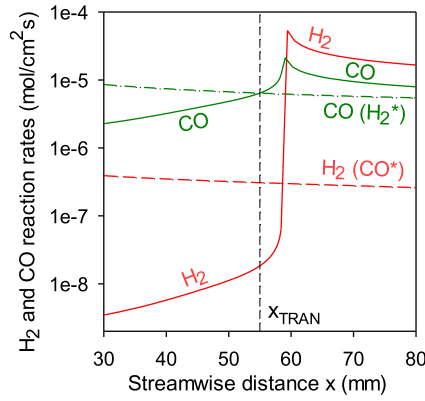
Fig. 8. Computed axial profiles of the H_2 and CO catalytic reaction rate magnitudes at the lower wall of Case 6. Solid lines: standard simulations. Dashed lines: simulations with chemically inert species H_2^* and CO^*.
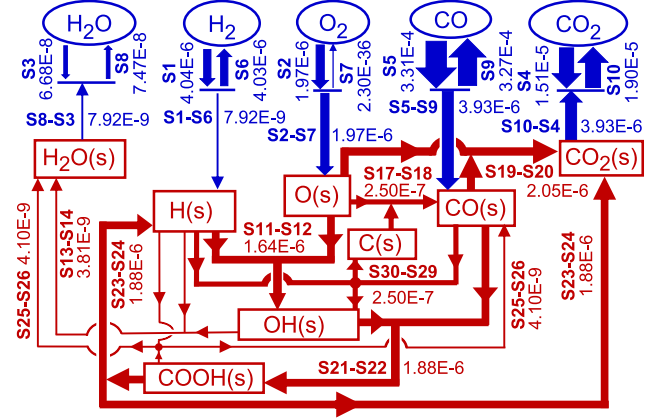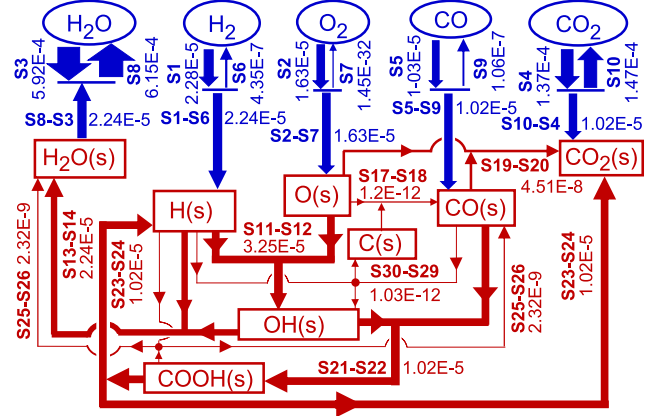

Fig. 9. Computed reaction fluxes at the lower wall of Case 6 at two locations: (a) before transition, $x = 45$ mm, (b) after transition, $x = 65$ mm (units: mol/cm^{2}s).

behavior. Obviously, such an extreme stretching led to a large scatter in the Raman data due to measurement uncertainty. The normal computations (solid lines) at these upstream positions indicated a negative (positive) H_2 gradient at the lower (upper) wall. Although this appeared counterintuitive by suggesting a net catalytic production of H_2, it was a result of thermal diffusion. The transverse $(-y)$ diffusion velocity component, $V_{H2, y}$, within the mixture-average-diffusion transport model of Eq. (3) becomes:

$$V_{H2,y} = -D_{H2,m} \frac{1}{X_{H2}} \frac{\partial X_{H2}}{\partial y} - \frac{D_{H2}^T}{\rho Y_{H2}} \frac{1}{T} \frac{\partial T}{\partial y}, \qquad (4)$$

with $D_{H2,m}$ and D_{H2}^T the mixture-average diffusion and thermal diffusion coefficients of hydrogen, respectively. Since for the light hydrogen molecule $D_{H2}^T < 0$ [38] and as the walls were always hotter than the gas, e.g. $(\partial T/\partial y)_{y=0} < 0$ at the lower wall, the condition $(\partial X_{H2}/\partial y)_{y=0} < 0$ was necessary to obtain a solution with vanishingly small surface reaction rate, which was equivalent to $(V_{H2,y})_{y=0} \approx 0$ (given the interfacial boundary condition $(V_{H2,y})_{y=0} \sim (\dot{s}_{H2})_{y=0}$ in Eq. (1)). In other words, for very small hydrogen catalytic reaction rates both Fickian and thermal diffusion processes were important.

Comparisons of the standard CO computations (solid lines) to CO computations with the artificial H_2^* species (dashed lines), revealed transition temperatures (T_{TRAN}) below which H_2 inhibited the oxidation of CO and above which H_2 promoted the oxidation of CO. For example, at $x = 51$ mm in Fig. 7(a2) the dashed lines clearly indicated a much higher reactivity of CO when using inert H_2^* (see the much lower mole fractions of CO at the walls and the steeper CO transverse wall gradients), while at the next axial location $x = 66$ mm (Fig. 7(a3)) and at the lower wall ($y = 0$) the CO reactivity was somewhat higher in the simulations with standard H_2 (see circled area at the lower wall in Fig. 7(a3)). At about the same axial positions H_2 exhibited a similar behavior: the presence of CO inhibited H_2 oxidation at $x = 51$ mm (Fig. 7(a6)) and promoted H_2 oxidation at $x = 66$ mm (see circled area in Fig. 7(a7)). The transition temperature for Case 6, calculated from the simulation results at the lower wall, was $T_{TRAN} = 549$ K and occurred at $x_{TRAN} = 55$ mm. This behavior is summarized in Fig. 8, providing the computed magnitudes of the catalytic reaction rates $\dot{s}_{H2}$ and $\dot{s}_{CO}$ at the lower wall for Case 6. The H_2 inhibition on CO oxidation was evident, as for $x < x_{TRAN}$ the CO reaction rates in the standard simulations were lower than the corresponding ones with chemically inert H_2^* species. On the other hand, CO inhibited the H_2 oxidation for $x < 58.5$ mm and CO promoted the H_2 oxidation for $x \geq 58.5$ mm (with 58.5 mm being somewhat longer than x_{TRAN}). This is also seen in Fig. 8, where for $x \geq 58.5$ mm the reaction rate
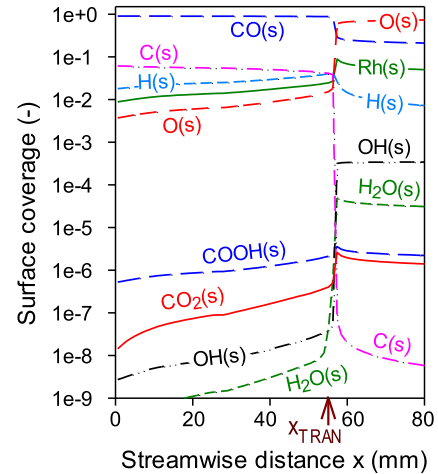

Fig. 10. Computed surface coverage at the lower wall of Case 6.

of H_2 in the standard simulations overtook the reaction rate of H_2 computed when considering a chemically inert species CO^*.

The underlying processes before and after the transition position are elaborated next. For the lower wall of Case 6, Figs. 9 and 10 provide reaction flux diagrams at two axial locations upstream and downstream of x_{TRAN} and the surface coverage, respectively. For $x = 45$ mm ($< x_{TRAN} = 55$ mm) in Fig. 9(a), the direct CO oxidation pathway $O(s) + CO(s) \rightarrow CO_2(s)$ (net of reactions S19-S20) was of the same order of magnitude as the indirect oxidation pathway
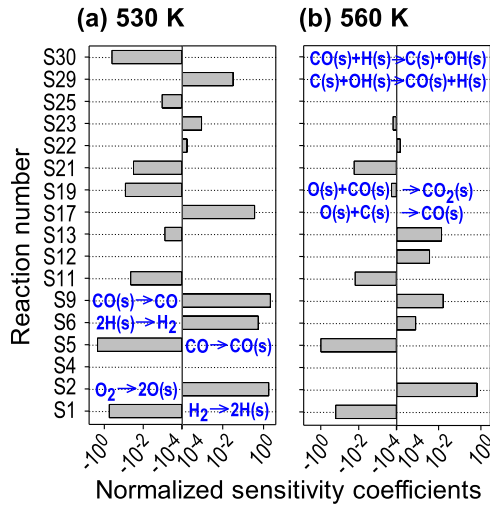
Fig. 11. Normalized sensitivity coefficients of controlling reactions (reaction numbering follows Table SM1) on CO, obtained in a SPSR with the inlet composition of Case 6 and temperature: (a) 530 K, and (b) 560 K.
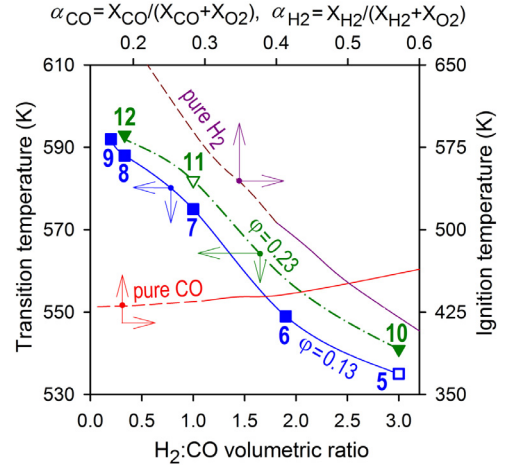

Fig. 12. Transition temperatures T_{TRAN} for Cases 5-12 in Table 1 (open symbols denote upper limits for T_{TRAN}) and ignition temperatures of pure CO and H_2 versus α from [41].

via carboxyl reactions: CO(s)+OH(s) → COOH(s) (S21-S22) followed by COOH(s) → CO₂(s)+H(s) (S23-S24). However, for $x = 65$ mm ($> x_{TRAN}$) in Fig. 9(b) the direct CO oxidation pathway (S19-S20) was negligible compared to the indirect pathway (S23-S24). This was because at $x < x_{TRAN}$ the H_2 reactions were not ignited (see the minimal net H_2 reaction rate (S1–S6) in Fig. 9(a)) such that OH(s), which was required to initiate the indirect CO oxidation route, was minor upstream of x_{TRAN} (see Fig. 10).

At $x < x_{TRAN}$ temperatures were low enough such that the main surface coverage was CO(s) –given the higher sticking coefficient of CO compared to either H_2 or O_2 (see S1, S2 and S5 in Table SM1). As the surface temperature increased along the wall, the net adsorptive reactions of H_2 (S1-S6) and especially of O_2 (S2-S7) were favored such that O(s) and H(s) gradually increased and thus OH(s) was also built via O(s)+H(s) → OH(s) (S11-S12) as evidenced in Fig. 10. Once OH(s) grew to appreciable amounts, the indirect oxidation pathway via COOH(s) became the dominant CO oxidation route. The indirect CO oxidation pathway was in turn much faster than the direct one, such that at $x > x_{TRAN}$ the consumption of CO was always to transport-limited as evidenced from the CO profiles of all cases in Fig. 7.

Figure 11 provides the normalized sensitivity coefficients for CO at temperatures of 530 K and 560 K (below and above $T_{TRAN} = 549$ K, respectively) obtained using the surface perfectly stirred reactor (SPSR) package of Chemkin [43]. The inlet composition was the same as in Case 6, while the SPSR surface-to-volume (S/V) ratio and the residence time were 33 cm^{-1} and 40 ms, respectively. The direct oxidation reaction S19 as well as the C(s)-containing reactions (S17, S29 and S30) were important at 530 K ($< T_{TRAN}$) but insignificant at 560 K ($> T_{TRAN}$). For both temperatures the H_2, CO, and O_2 adsorption reactions (S1, S5 and S2) were important, while the H_2 and CO desorption reactions (S6 and S9) were mainly important for 530 K (note the logarithmic abscissa in Fig. 11). The SA results before and after transition obtained in Fig. 11 using the SPSR tool were consistent with the reaction flux diagrams in Fig. 9 obtained in the channel reactor prior to and after transition. This happened despite the fact that after transition there were strong transport limitations in the channel reactor, especially for CO.

Transition temperatures for Cases 7 and 8 in Fig. 7(b, c), calculated in a similar fashion as Case 6, were 575 K and 588 K, respectively. For all Cases 5–9 having $\varphi = 0.13$, T_{TRAN} dropped monotonically with increasing H_2:CO ratio as shown in Fig. 12. For Case
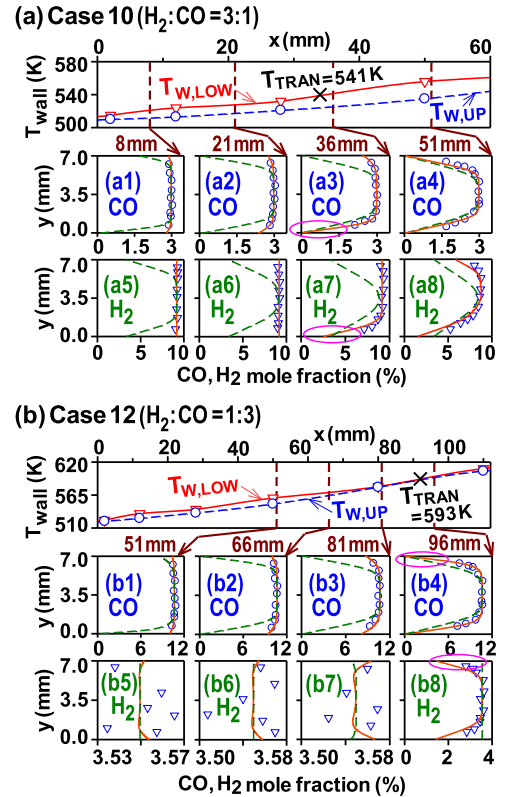

Fig. 13. Measured wall temperatures (circles: upper-wall, triangles: lower-wall) with fitted profiles (lines), and comparisons between Raman-measured (symbols) and predicted (solid lines) transverse profiles of CO and H_2 mole fractions, Cases 10 and 12. Line notation as in Fig. 7.

5 with H_2:CO = 3:1, the wall temperatures were not low enough (minimum value $T_{w,min} = 535$ K) to observe an inhibition such that H_2 always promoted the CO oxidation. Hence, for Case 5 the $T_{w,min}$ is plotted in Fig. 12 and only defines an upper limit for T_{TRAN}.

For the larger $\varphi = 0.23$, transition temperatures T_{TRAN} were always higher than those for $\varphi = 0.13$ at the same H_2:CO ratios (see Cases 10 and 12 in Fig. 13 and also summary plot in Fig. 12). This was due to the higher O_2 content of the $\varphi = 0.13$ cases (see Table 1) which facilitated ignition and led to lower T_{TRAN}. For example, in Case 8 ($\varphi = 0.13$) O(s) was 0.00685 for 580 K and 0.00499
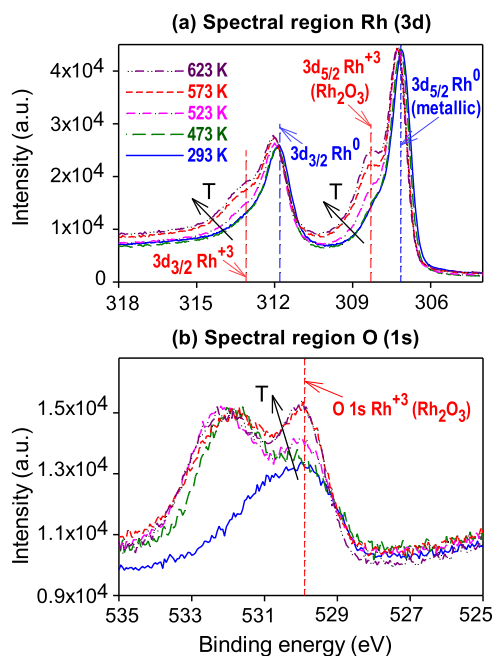
Fig. 14. XPS spectra of Rh samples at various temperatures, (a) Rh 3d and (b) O 1 s regions.

Fig. 15. SEM images of Rh samples heated in air at various temperatures.

for 575 K, while for Case 12 ($\varphi = 0.23$) the corresponding values were 0.00336 and 0.00211. For Case 11 with H_2:CO = 1:1, only an upper limit for T_{TRAN} could be defined as the wall temperatures were too high to observe an H_2-induced inhibition of CO oxidation. The deduced T_{TRAN} were always higher than literature ignition temperatures for pure CO [41] (see Fig. 12 and note the different ordinate scales). It is noted here that α_{H2} or α_{CO} were appropriate parameters only for describing pure H_2 or CO fuels.

Transition temperatures were essentially light-off temperatures for CO, since for $T_w < T_{TRAN}$ the CO conversions were kinetically controlled, while for $T_w > T_{TRAN}$ they were transport-limited (see Figs. 7 and 13). For hydrogen, however, T_{TRAN} always defined transition from a practically non-reacting state to a kinetically-controlled H_2 conversion.

4.3. Surface analysis

XPS spectra for the fresh and heated samples are illustrated in Fig. 14 for the Rh 3d and O 1 s regions. The Rh 3d spectra in Fig. 14(a) indicated mixed metallic (Rh^0) and oxidized Rh_2O_3 (Rh^{+3}) phases for all samples, with the Rh^{+3} phase progressively increasing as the temperature increased. The Rh 3d transitions in Fig. 14(a) indicated $3d_{5/2}$ at 307.2 and 308.3 eV for Rh^0 and Rh^{+3}, respectively; similarly, $3d_{3/2}$ was at 311.8 and 313.1 eV for Rh^0 and Rh^{+3}, respectively [44]. The increased Rh_2O_3 (Rh^{+3}) phase with rising temperature was also matched by the O(1 s) peak at 529.9 eV in Fig. 14(b). The additional feature at ~532 eV in the O 1 s spectra Fig. 14(b) was mainly RhO_2 [45].

The increased oxidation towards Rh_2O_3 with rising temperatures has also been reported during Rh oxidation in O_2/Ar mixtures over the range 323–573 K in [45,46]. In particular, the observed weak oxidation at the investigated temperatures in Fig. 14 is in agreement with XPS data in [46]. This has implications for the kinetic modeling, as a strong oxidation from Rh^0 to Rh^{+3} may have necessitated a more complex reaction mechanism (with more than one active sites) in order to capture the light-off behavior and the underlying H_2/CO hetero-/homogeneous chemistry interactions.
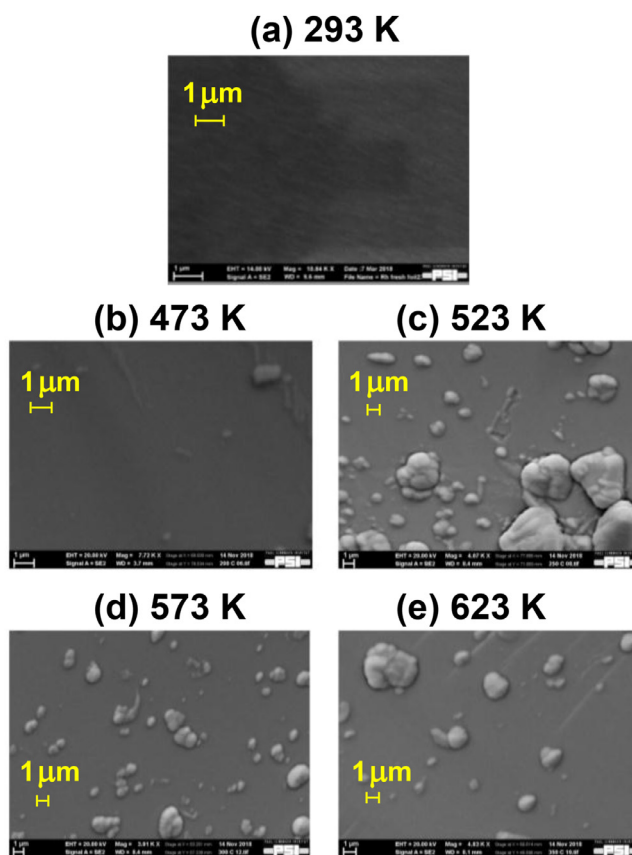
The increased surface oxidation with rising temperature was further supported by the elemental EDS analysis (see supplemental Fig. SM1) –notwithstanding the qualitative nature of the EDS technique. The SEM images for the five Rh samples are illustrated in in Fig. 15. Increased heating initiated the formation of mostly spherical particles with sizes 1-10 μm and a low density of defects (Fig. 15(c–e)). The polycrystalline nature of the surface of the as-prepared sample can be deduced from Fig. 15(a). The low number of defects with increasing temperature further suggests small overall changes in the active surface area of the catalyst.

4.4. Implications for practical syngas-fueled catalytic reactors

Quantification of the transition temperatures T_{TRAN} is presented in the numerical results of Fig. 16, which were obtained with the SPSR code of Chemkin [43] for the compositions in Table 1 at 5 bar. An additional composition H_2:CO = 5:1 (not included in Table 1) is shown, created by replacing part of N_2 in the H_2:CO = 3:1 cases with H_2. T_{TRAN} depended on the inlet mixture composition and on the product of the reactor surface-to-volume ratio (S/V) and residence time (τ) since the gas-phase species SPSR governing equations were $\rho(Y_{k,\text{IN}} - Y_{k,\text{OUT}}) = (S/V)\tau \dot{s}_k W_k$. For a given product $(S/V)\tau$, T_{TRAN} was computed by gradually increasing the SPSR temperature and finding the lowest possible temperature for which the CO conversion obtained with H_2/CO exceeded the corresponding one with H_2*/CO mixture. Computed T_{TRAN} decreased monotonically with increasing $(S/V)\tau$, while for a given $(S/V)\tau$ they decreased with rising H_2:CO ratio and dropping equivalence ratio. The highest H_2:CO ratio 5:1 and lowest $\varphi = 0.13$ were the most favorable, yielding the lowest T_{TRAN}.

In practical power-generation catalytic burners, the product $(S/V)\tau$ is typically ~0.4-2.0 s/cm [11] (shown with shaded area in
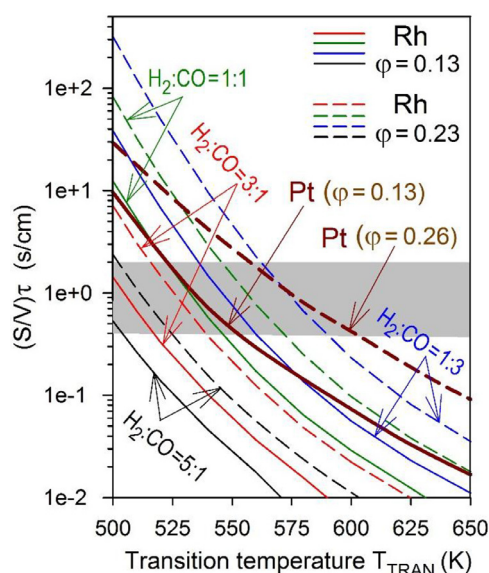
Fig. 16. SPSR transition temperatures versus the product of surface-to-volume ratio (S/V) and residence time τ. Shaded area shows $(S/V)\tau$ regimes in power generation while the thick lines are corresponding predictions for platinum [22].

Fig. 16); over this $(S/V)\tau$ range of industrial interest, temperatures 500–590 K were required to fully ignite the CO oxidation. There were key differences with the Pt behavior under similar operating conditions [22]. In [22] the two investigated equivalence ratios were $\varphi = 0.13$ and 0.26. T_{TRAN} was, for a given φ, strongly dependent on H_2:CO ratio for Rh and very weakly for Pt, while for a given H_2:CO ratio T_{TRAN} was moderately dependent on φ for Rh and stronger for Pt. The Pt solutions for $\varphi = 0.13$ and 0.26 are also shown in Fig. 16 with thick lines. No dependence on H_2:CO ratio is shown for Pt, as the extreme H_2:CO ratios extended +/- 8 K around the provided Pt lines. For the shaded area of power generation systems, T_{TRAN} on Pt spanned the narrow range 523–552 K at $\varphi = 0.13$, while the corresponding T_{TRAN} on Rh spanned the much wider range 502–590 K. For $\varphi = 0.26$ on Pt T_{TRAN} was in the range 558–602 K, while for $\varphi = 0.23$ on Rh the range was 525–591 K. Given the strong impact of H_2:CO ratio on Rh, high-H_2-content syngas (produced by efficient fuel decarbonization, $H_2 > 80\%$ vol.) was clearly desirable for this catalyst. However, for low H_2:CO ratios ($\leq$ 1:3, as in coal gasification applications) Pt was the preferred catalyst.

5. Conclusions

The kinetic interactions of CO and H_2 on Rh were investigated in a channel-flow catalytic reactor at surface temperatures 510–610 K (a range crucial for part-load/idling conditions in gas turbines and for recuperative micro-turbine-based microreactors). Experiments were performed for pure H_2 and CO fuels as well as for H_2/CO blends with H_2:CO volumetric ratios 1:5–3:1, overall equivalence ratios $\varphi = 0.13$ and 0.23, and pressure of 5 bar. In situ Raman measurements provided the transverse profiles of major gas-phase species concentrations above the catalyst, while surface science analysis (XPS, SEM/EDS) determined the oxidation state and morphology of the catalyst surface. Numerical simulations were performed using a 2-D NS code with a detailed catalytic mechanism and realistic transport. The following are the key conclusions of this study.

(1) Measurements and simulations have attested that the catalytic ignition of pure CO was nearly independent of the CO concentration (or equivalence ratio) for the presently investigated low mole-fraction ratios $\alpha_{CO} = X_{CO}/(X_{CO}+X_{O2}) \leq 0.31$. On the other hand, the ignition of pure H_2 was promoted by increased hydrogen concentration for the investigated ratios $\alpha_{H2} = X_{H2}/(X_{H2}+X_{O2}) \leq 0.32$. Comparisons of Raman measurements and predictions were in good agreement for pure CO oxidation, while for pure H_2 oxidation the catalytic reactivity was slightly overpredicted.

(2) Comparison of measurements and simulations for H_2/CO blends, attested the overall suitability of the employed catalytic reaction mechanism. Transition temperatures T_{TRAN} below (above) which H_2 inhibited (promoted) the CO oxidation have been assessed. Likewise, CO inhibited (promoted) the H_2 oxidation below (above) a temperature that was slightly higher than T_{TRAN}.

(3) The deduced transition temperatures T_{TRAN} decreased with increasing H_2:CO ratio and decreasing φ. For a given φ, T_{TRAN} strongly depended on H_2:CO ratio while for a given H_2:CO ratio the φ-dependence of T_{TRAN} was weak. The H_2/CO kinetic interactions responsible for this behavior originated from the dominant CO(s), C(s) and H(s) coverage at $T < T_{TRAN}$ and the corresponding low O(s) coverage that led to a slow conversion of CO(s) via the direct oxidation pathway CO(s) + O(s) → CO_2(s). However, as temperature increased to $T > T_{TRAN}$ the adsorption of H_2 and especially of O_2 were favored such that O(s) and H(s) gradually increased and OH(s) was built via O(s) + H(s)→ OH(s). As OH(s) grew to significant amounts, the indirect oxidation pathway via carboxyl reactions (CO(s) + OH(s)→ COOH(s) followed by COOH(s) → CO_2(s) + H(s)) became the dominant CO oxidation route. The indirect oxidation pathway was, in turn, very efficient in converting CO(s).

(4) The observed H_2 and CO kinetic interactions suggested using high H_2:CO ratio fuels (e.g. produced by an efficient hydrocarbon decarbonization in IGCC power plants) when employing rhodium as catalyst. This behavior was opposite to that of Pt, whereby the dependence of T_{TRAN} on H_2:CO ratio was weak and hence this catalyst was suited for applications with low H_2:CO ratio fuels, such as syngas produced via coal gasification.

(5) Surface science analysis by XPS and EDS revealed that the Rh catalyst was progressively oxidized as the temperature increased from 293 K to 623 K. Surface morphology studies by SEM indicated the formation of nearly spherical particles with sizes 1-10 μm and low defect density on the heated samples.

Supplementary material

Supplementary material associated with this article can be found, in the online version, at doi:10.1016/j.combustflame.2019.01.021.

References

[1] C.C. Cormos, Integrated assessment of IGCC power generation technology with carbon capture and storage (CCS), Energy 42 (2012) 434–445.

[2] L.O. Nord, R. Anantharaman, O. Bolland, Design and off-design analyses of a pre-combustion CO_2 capture process in a natural gas combined cycle power plant, Int. J. Greenh. Gas Con. 3 (2009) 385–392.

[3] M.C. Romano, P. Chiesa, G. Lozza, Pre-combustion CO_2 capture from natural gas power plants, with ATR and MDEA processes, Int. J. Greenh. Gas Con. 4 (2010) 785–797.

[4] N.S. Kaisare, D.G. Vlachos, A review on microcombustion: fundamentals, devices and applications, Prog. Energy Combust. Sci. 38 (2012) 321–359.

[5] R. Sui, E. Es-sebbar, J. Mantzaras, N.I. Prasianakis, Experimental and numerical investigation of fuel-lean H_2/CO/air and H_2/CH_4/air catalytic microreactors, Combust. Sci. Technol. 190 (2018) 336–362.

[6] R.A. Dalla Betta, T. Rostrup-Nielsen, Application of catalytic combustion to a 1.5 MW industrial gas turbine, Catal. Today 47 (1999) 369–375.

[7] R. Carroni, T. Griffin, J. Mantzaras, M. Reinke, High-pressure experiments and modeling of methane/air catalytic combustion for power generation applications, Catal. Today 83 (2003) 157–170.

[8] S. Eriksson, A. Schneider, J. Mantzaras, M. Wolf, S. Jaras, Experimental and numerical investigation of supported rhodium catalysts for partial oxidation of methane in exhaust gas diluted reaction mixtures, Chem. Eng. Sci. 62 (2007) 3991–4011.

[9] J. Mantzaras, Catalytic combustion of syngas, Combust. Sci. Technol. 180 (2008) 1137–1168.

[10] Y. Ghermay, J. Mantzaras, R. Bombach, Experimental and numerical investigation of hetero-/homogeneous combustion of $CO/H_2/O_2/N_2$ mixtures over platinum at pressures up to 5 bar, Proc. Combust. Inst. 33 (2011) 1827–1835.

[11] F. Bolaños, D. Winkler, F. Piringer, T. Griffin, R. Bombach, J. Mantzaras, Study of a rich/lean staged combustion concept for hydrogen at gas turbine relevant conditions, ASME GT2013-94420, 2013 June 3-7.

[12] J. Mantzaras, C. Appel, Effects of finite rate heterogeneous kinetics on homogeneous ignition in catalytically stabilized channel-flow combustion, Combust. Flame 130 (2002) 336–351.

[13] A. Schlegel, S. Buser, P. Benz, H. Bockhorn, F. Mauss, NOx Formation in lean premixed non-catalytic and catalytically stabilized combustion of propane, 25th Symp. (Int.) Combust. (1994) 1019–1026.

[14] A. Schlegel, P. Benz, T. Griffin, W. Weisenstein, H. Bockhorn, Catalytic stabilization of lean premixed combustion: method for improving NOx emissions, Combust. Flame 105 (1996) 332–340.

[15] G. Pizza, J. Mantzaras, C.E. Frouzakis, A.G. Tomboulides, K. Boulouchos, Suppression of combustion instabilities of premixed hydrogen/air flames in microchannels using heterogeneous reactions, Proc. Combust. Inst. 32 (2009) 3051–3058.

[16] G. Pizza, J. Mantzaras, C.E. Frouzakis, Flame dynamics in catalytic and non-catalytic mesoscale microreactors, Catal. Today 155 (2010) 123–130.

[17] B. Schneider, M. Bruderer, D. Dyntar, C. Zwyssig, M. Diener, K. Boulouchos, R.S. Abhari, L. Guzzella, J.W. Kolar, Ultra-high-energy-density converter for portable power, Power-MEMS 2005, Tokyo, Japan, 2005 November 28-30.

[18] S. Salomons, M. Votsmeier, R. Hayes, A. Drochner, H. Vogel, J. Gieshof, CO and H_2 oxidation on a platinum monolith diesel oxidation catalyst, Catal. Today 117 (2006) 491–497.

[19] J.A. Federici, D.G. Vlachos, Experimental studies on syngas catalytic combustion on Pt/Al_2O_3 in a microreactor, Combust. Flame 158 (2011) 2540–2543.

[20] J. Mantzaras, Progress in non-intrusive laser-based measurements of gas-phase thermoscalars and supporting modeling near catalytic interfaces, Prog. Energy Combust. Sci. 70 (2019) 169–211.

[21] X. Zheng, M. Schultze, J. Mantzaras, R. Bombach, Effects of hydrogen addition on the catalytic oxidation of carbon monoxide over platinum at power generation relevant temperatures, Proc. Combust. Inst. 34 (2013) 3343–3350.

[22] X. Zheng, J. Mantzaras, R. Bombach, Kinetic interactions between hydrogen and carbon monoxide oxidation over platinum, Combust. Flame 161 (2014) 332–346.

[23] K.W. Beebe, K.D. Cairns, V.K. Pareek, S.G. Nickolas, J.C. Schlatter, T. Tsuchiya, Development of catalytic combustion technology for single-digit emissions from industrial gas turbines, Catal. Today 59 (2000) 95–115.

[24] M. Bhagiyalakshmi, R. Anuradha, S.D. Park, T.S. Park, W.S. Cha, H.T. Jang, Effect of bimetallic Pt-Rh and trimetallic Pt-Pd-Rh Catalysts for low temperature catalytic combustion of methane, Bull. Korean Chem. Soc. 31 (2010) 120–124.

[25] A. Maione, F. Andre, P. Ruiz, The effect of Rh addition on Pd/γ-Al_2O_3 catalysts deposited on FeCrAlloy fibers for total combustion of methane, Appl. Catal. A–Gen. 333 (2007) 1–10.

[26] A.B. Mhadeshwar, D.G. Vlachos, Hierarchical, multiscale surface reaction mechanism development: CO and H_2 oxidation, water-gas shift, and preferential oxidation of CO on Rh, J. Catal 234 (2005) 48–63.

[27] M. Maestri, A. Beretta, T. Faravelli, G. Groppi, E. Tronconi, D.G. Vlachos, Two-dimensional detailed modeling of fuel-rich H_2 combustion over Rh/Al_2O_3 catalyst, Chem. Eng. Sci. 63 (2008) 2657–2669.

[28] H. Karadeniz, C. Karakaya, S. Tischer, O. Deutschmann, Numerical modeling of stagnation-flows on porous catalytic surfaces: CO oxidation on Rh/Al_2O_3, Chem. Eng. Sci. 104 (2013) 899–907.

[29] C. Hauck, S. Tischer, L. Maier, O. Deutschmann, Modelling of local aging effects of commercial three-way catalysts: spatial temperature and CO conversion profiles, Can. J. Chem. Eng. 92 (2014) 1587–1596.

[30] R. Sui, E. Es-Sebbar, J. Mantzaras, R. Bombach, Homogeneous ignition during fuel-rich $H_2/O_2/N_2$ combustion in platinum-coated channels at elevated pressures, Combust. Flame 180 (2017) 184–195.

[31] M. Reinke, J. Mantzaras, R. Schaeren, R. Bombach, A. Inauen, S. Schenker, High-pressure catalytic combustion of methane over platinum: in situ experiments and detailed numerical predictions, Combust. Flame 136 (2004) 217–240.

[32] P.A. Bui, D.G. Vlachos, P.R. Westmoreland, Homogeneous ignition of hydrogen/air mixtures over platinum, 26th Symp. (Int.) Combust. (1996) 1763–1770.

[33] C. Appel, J. Mantzaras, R. Schaeren, R. Bombach, A. Inauen, B. Kaeppeli, B. Hemmerling, A. Stampanoni, An experimental and numerical investigation of homogeneous ignition in catalytically stabilized combustion of hydrogen/air mixtures over platinum, Combust. Flame 128 (2002) 340–368.

[34] Y. Ghermay, J. Mantzaras, R. Bombach, Effects of hydrogen preconversion on the homogeneous ignition of fuel-lean $H_2/O_2/N_2/CO_2$ mixtures over platinum at moderate pressures, Combust. Flame 157 (2010) 1942–1958.

[35] C. Karakaya, L. Maier, O. Deutschmann, Surface reaction kinetics of the oxidation and reforming of CH_4 over Rh/Al_2O_3 catalysts, Int. J. Chem. Kinet. 48 (2016) 144–160.

[36] C. Karakaya, O. Deutschmann, Kinetics of hydrogen oxidation on Rh/Al_2O_3 catalysts studied in a stagnation-flow reactor, Chem. Eng. Sci. 89 (2013) 171–184.

[37] J. Li, Z.W. Zhao, A. Kazakov, M. Chaos, F.L. Dryer, J.J. Scire, A comprehensive kinetic mechanism for CO, CH_2O, and CH_3OH combustion, Int. J. Chem. Kinet. 39 (2007) 109–136.

[38] R.J. Kee, G. Dixon-Lewis, J. Warnatz, M.E. Coltrin, J.A. Miller, A Fortran computer code package for the evaluation of gas-phase multicomponent transport properties, Report No. SAND86-8246, Sandia National Laboratories, 1996.

[39] M.E. Coltrin, R.J. Kee, F.M. Rupley, Surface Chemkin: a Fortran package for analyzing heterogeneous chemical kinetics at the solid surface-gas phase interface, Report No. SAND90-8003C, Sandia National Laboratories, 1996.

[40] R.J. Kee, F.M. Rupley, J.A. Miller, Chemkin II: A Fortran chemical kinetics package for the analysis of gas-phase chemical kinetics, Report No. SAND89-8009B, Sandia National Laboratories, 1996.

[41] J.N. Bär, C. Karakaya, O. Deutschmann, Catalytic ignition of light hydrocarbons over Rh/Al_2O_3 studied in a stagnation-point flow reactor, Proc. Combust. Inst. 34 (2013) 2313–2320.

[42] O. Deutschmann, R. Schmidt, F. Behrendt, J. Warnatz, Numerical modeling of catalytic ignition, 26th Symp. (Int.) Combust. (1996) 1747–1754.

[43] H.K. Moffat, R.J. Kee, J.F. Grcar, J.A. Miller, Surface PSR: A Fortran program for modeling well-stirred reactors with gas and surface reactions, Report No. SAND91-8001, Sandia National Laboratories, 1993.

[44] Y. Abe, K. Kato, M. Kawamura, K. Sasaki, Rhodium and rhodium oxide thin films characterized by XPS, Surf. Sci. Spectra 8 (2001) 117–125.

[45] A.A. Tolia, R.J. Smiley, W.N. Delgass, C.G. Takoudis, M.J. Weaver, Surface oxidation of rhodium at ambient pressures as probed by surface-enhanced Raman and X-ray photoelectron spectroscopies, J. Catal. 150 (1994) 56–70.

[46] A. Muñoz, G. Munuera, P. Malet, A.R. González-Elipe, J.P. Espinós, XPS and TPR/TPO study of the behavior of rhodium particles supported on TiO_2, Surf. Interface Anal. 12 (1988) 247–252.